EPJ E
Soft Matter and Biological Physics
EPJ.org
your physics journal

Eur. Phys. J. E (2017) **40**: 97 DOI 10.1140/epje/i2017-11587-3

Image windowing mitigates edge effects in Differential Dynamic Microscopy

Fabio Giavazzi, Paolo Edera, Peter J. Lu and Roberto Cerbino

edp sciences Società Italiana di Fisica Springer

Eur. Phys. J. E (2017) **40**: 97
DOI 10.1140/epje/i2017-11587-3

THE EUROPEAN PHYSICAL JOURNAL E

Tips and Tricks

Image windowing mitigates edge effects in Differential Dynamic Microscopy*

Fabio Giavazzi[1,a], Paolo Edera[1], Peter J. Lu[2], and Roberto Cerbino[1,b]

[1] Dipartimento di Biotecnologie Mediche e Medicina Traslazionale, Università degli Studi di Milano, via F.lli Cervi 93, 20090 Segrate, Italy
[2] Department of Physics and SEAS, Harvard University, Cambridge, MA 02138, USA

Received 15 July 2017 and Received in final form 20 September 2017
Published online: 9 November 2017 –

Abstract. Differential Dynamic Microscopy (DDM) analyzes traditional real-space microscope images to extract information on sample dynamics in a way akin to light scattering, by decomposing each image in a sequence into Fourier modes, and evaluating their time correlation properties. DDM has been applied in a number of soft-matter and colloidal systems. However, objects observed to move out of the microscope's captured field of view, intersecting the edges of the acquired images, can introduce spurious but significant errors in the subsequent analysis. Here we show that application of a spatial windowing filter to images in a sequence before they enter the standard DDM analysis can reduce these artifacts substantially. Moreover, windowing can increase significantly the accessible range of wave vectors probed by DDM, and may further yield unexpected information, such as the size polydispersity of a colloidal suspension.

1 Introduction

Differential Dynamic Microscopy (DDM) uses Fourier analysis of microscope image sequences to characterize the structure and dynamics of a wide variety of physical and biological systems [1], including dilute isotropic [2,3] and anisotropic [4,5] colloidal particles, dense colloidal suspensions [6–8], molecular [9] and complex [10,11] fluids, motile microorganisms [6,12,13], and sub-cellular structures [14, 15]. This broad adoption of DDM stems from its numerous advantages [16], including simple implementation with ordinary microscopy, no need for custom instrumentation, insensitivity to normal amounts of dirt or multiple scattering, and an ability to focus on regions of interest in images collected with a variety of image-contrast mechanisms: bright field [2], dark field [3], phase contrast [12], wide field fluorescence [17], polarized [5,11], differential interference contrast [14], light sheet [18] and confocal microscopy (ConDDM) [6–8].

Theoretically, DDM probes a range of wave vectors q that is determined by two factors: the lower bound $q_{\mathrm{min,th}} = 2\pi/L$ is constrained by the image size L, while the upper bound $q_{\mathrm{max,th}} = \pi/a$ is controlled by the pixel size a. In real experiments, the practical range $[q_{\mathrm{min}}, q_{\mathrm{max}}]$ for which the statics and the dynamics can be measured reliably is often more limited. Limitations can arise from both the statics (*e.g.*, the signal to noise ratio is too low) and the dynamics (*e.g.*, the observation time window is too short to adequately sample the dynamics associated with the slowest modes, or the temporal resolution is too poor to capture the faster dynamics, typically associated with the smaller length scales). Other relevant practical limitations may result from mechanical drifts, vibrations or advective/convective flows driven by thermal inhomogeneities or pressure imbalance. We note that most of these limitations are by no means unique to DDM, as other methods (*e.g.*, particle tracking) are also affected for instance by a poor temporal resolution, vibrations and mechanical/convective drifts.

An additional limitation constraining the range of probed wave vectors arises from the fact that, in any sequence of images with finite size, particles crossing the edge of the image boundary will be imaged only partially. Thus, the images contain particles with straight, sharp edges that, as is well known in signal processing theory [19], create significant artifacts in the static Fourier spectrum. This effect is particularly pronounced in systems with limited spatial bandwidth, as is common in microscope images due to the resolution constraints imposed by the diffraction limit. Although, thus far, this problem has been given little attention, it nonetheless leads to spurious artifacts in the Fourier transforms of the images, thereby potentially affecting also the DDM results for the

* Supplementary material in the form of a .avi file available from the Journal web page at
http://dx.doi.org/10.1140/epje/i2017-11587-3

[a] e-mail: fabio.giavazzi@unimi.it
[b] e-mail: roberto.cerbino@unimi.it

sample dynamics, though the specific effects have not yet been established.

In this paper, we combine theory and experiments to show that the partial imaging of particles at the boundary, inevitable for all images of finite size, introduces significant artifacts, namely a spurious, nearly-q-independent secondary decay in the DDM image structure functions. This decay, present in principle for all q, dominates the dynamics at the largest q values, where the signal associated with particle dynamics vanishes due to the particle form factor $P(q)$. We mitigate this artifact with a simple preprocessing step: spatial windowing (apodization) of the images, which does not increase substantially computational complexity, yet increases significantly $q_{\max}$. The expansion of the accessible range of q values not only improves the accuracy of DDM in general, but also opens up new analyses in specific cases; for example, we show how windowing may enable the estimation of size polydispersity in a colloidal suspension using a method common in Dynamic Light Scattering (DLS) experiments [20,21]. Remarkably, we show that this artifact also arises with molecular fluids, as a consequence of the limits imposed by diffraction on the detection of sub-wavelength entities.

2 Boundary effects in dynamic microscopy

A detailed description of the image processing algorithm on which DDM is based can be found in refs. [22,2,23, 16]. In brief, a sequence of N digital images $I(\mathbf{x},t)$ is acquired, where $\mathbf{x} = a_0\,(n_x, n_y)$ and $t = n\Delta t_0$. Here a_0 is the effective pixel size (the physical pixel size divided by the objective magnification), n_x, n_y are integer numbers comprised between 1 and the image size M (assumed to be the same for both dimensions) and Δt_0 is the time interval between two consecutive images. The key quantity from which the dynamical information is extracted is the so-called image structure function $D(\mathbf{q},\Delta t)$, that is calculated as

$$D(\mathbf{q},\Delta t) = \left\langle \left| FFT\left[I(\mathbf{x},t_0+\Delta t) - I(\mathbf{x},t_0)\right]\right|^2 \right\rangle, \qquad (1)$$

where FFT indicates the Fast Fourier Transform operation and $\mathbf{q} = q_0\,(m_x, m_y)$, with m_x, m_y integers comprised between $-(\frac{M}{2}-1)$ and $\frac{M}{2}$. $q_0 = \frac{2\pi}{Ma_0}$. The expectation value $\langle\cdot\rangle$ is taken over time and, possibly, over different replicas of the same experiment.

For a linear space-invariant imaging process, the image structure function takes the form [23]

$$D(\mathbf{q},\Delta t) = A(\mathbf{q})\left[1 - f(\mathbf{q},\Delta t)\right] + B(\mathbf{q}), \qquad (2)$$

where $A(\mathbf{q})$ is an amplitude term that depends on the spatial intensity correlations present in the images and $B(\mathbf{q})$ accounts for the noise of the detection chain. The function $f(\mathbf{q},\Delta t) = f_{2D}(\mathbf{q},\Delta t) f_z(\mathbf{q},\Delta t)$ is defined in terms of a transverse part f_{2D} encoding dynamics in the image plane and an axial contribution f_z, which accounts for dynamics in the axial direction. In most cases of interest, such as for instance when the axial dynamics can be neglected or when small wave vectors are of interest, $f(\mathbf{q},\Delta t)$ coincides with the normalized intermediate scattering function probed by DLS [24,16].

Starting from eq. (2), the usual strategy in DDM experiments is based on

1) assuming a suitable functional form describing the time dependence of $f(\mathbf{q},\Delta t)$;
2) fitting the image structure function $D(\mathbf{q},\Delta t)$ to estimate the q-dependent parameters describing the relaxation of the different Fourier modes;
3) collecting together the results obtained at different q to extract the relevant quantity characterizing the dynamics and the statics of the sample.

For example, for a dispersion of dilute, non-interacting Brownian particles, the expected intermediate scattering function is $f(q,\Delta t) = \exp(-\Gamma(q)\Delta t)$. The fitting procedure provides an estimate of $\Gamma(q)$, whose expected scaling with q is $\Gamma(q) = D_t q^2$, where D_t is the translational diffusion coefficient of the particles. The best estimate for D_t is then obtained by a fit of $\Gamma(q)$. In this particular case, no structural correlations are expected, which means that the estimate for $A(\mathbf{q})$ provided by the fitting procedure provides information about the form factor $P(\mathbf{q})$ of the particles and the transfer function $T(\mathbf{q})$ of the optical setup [23]. In other cases, additional information about the structural correlations within the sample can be extracted [6,10,11].

Further insight can be obtained by making explicit the relationship between the sampled intensity $I(\mathbf{x},t)$ on the detector and the actual intensity $i(\mathbf{x},t)$ in the image plane as

$$I(\mathbf{x},t) = W_0(\mathbf{x})\left[i(\mathbf{x},t) + b(\mathbf{x},t)\right], \qquad (3)$$

which is helpful to account for finite sampling effects. Here, $W_0(\mathbf{x})$ is a window function that takes value 1 within the image boundaries and 0 outside and b is a detection noise term that we assume to be delta-correlated both in space and time.

In the following, we will focus on the case of a collection of N_p identical particles, whose positions are labeled by the coordinates $(\mathbf{x}_n, z_n)_{n=1,2,\ldots,N_p}$. For a linear, space-invariant imaging process [23], we obtain

$$i(\mathbf{x},t) = i_0 + \sum_n \psi\left(\mathbf{x} - \mathbf{x}_n(t), z_n(t)\right), \qquad (4)$$

where i_0 is the average intensity in the absence of the particles and ψ represents the intensity distribution associated with a single particle. In general, ψ is the result of the 2D convolution of the spatial distribution of the relevant optical parameter within the particle (*e.g.*, refractive index in the case of bright-field or dye density in the case of florescence microscopy) with the three-dimensional point-spread function of the microscope [23]. By introducing the spatial 2D Fourier transform of the function $g(\mathbf{x})$:

$$\hat{g}(\mathbf{q}) = \int_{-\infty}^{+\infty} \mathrm{d}x \int_{-\infty}^{+\infty} \mathrm{d}y g(\mathbf{x}) e^{-j\mathbf{q}\cdot\mathbf{x}} \qquad (5)$$

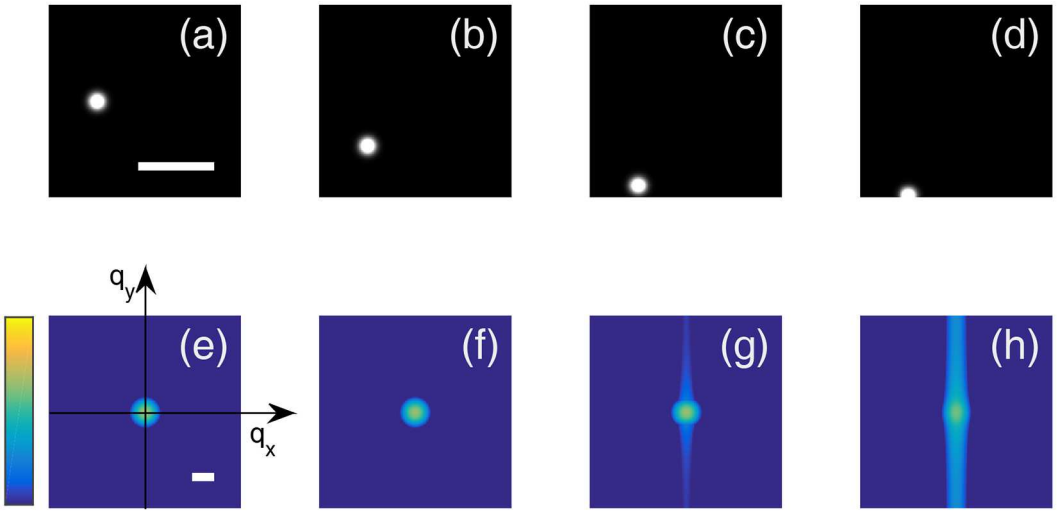

Fig. 1. Spectral leakage in DDM. A particle crossing image boundaries (top row) excites high-q wave vectors in the reconstructed Fourier spectrum (bottom row) along the direction perpendicular to the image boundary. Consequently, the characteristic dynamics associated with these events produce strong effects at large q. All images are simulated and represented using the same settings (image size: $N = 256$ pixels, effective particle radius: $\sigma_P = 10$ pixels), and Fourier spectra are represented on a logarithmic scale with the same color code. The size bar for real-space images shown in panel (a) corresponds to 100 pixels, while the size bar for Fourier-space images shown in panel (e) corresponds to $2\pi/\sigma_P$. A dynamic version of this figure is also available as supplementary movie M1.

we obtain after some manipulation the following expressions for the intermediate scattering function $f(\mathbf{q}, \Delta t)$ and the amplitude $A(\mathbf{q})$:

$$A(\mathbf{q}) = 2\tilde{N}_p P(\mathbf{q}) \tag{6}$$

and

$$f(\mathbf{q}, \Delta t) = \frac{|\hat{W}_0(\mathbf{q})|^2 * [f_\infty(\mathbf{q}, \Delta t) P_\infty(\mathbf{q})]}{P(\mathbf{q})}, \tag{7}$$

where $\tilde{N}_p$ is the average number of particles within the image and where we have defined the form factor

$$P(\mathbf{q}) = |\hat{W}_0(\mathbf{q})|^2 * P_\infty(\mathbf{q}) \tag{8}$$

and its limit for infinitely large samples

$$P_\infty(\mathbf{q}) = \langle |\hat{\psi}(\mathbf{q}, z)|^2 \rangle. \tag{9}$$

The noise term $B(\mathbf{q})$ is expected to be q independent and proportional to $\langle b^2 \rangle$. These equations describe how the statical and dynamical properties of particles, when reconstructed from the FFT analysis of the images, are affected by the presence of the boundaries and may differ from the ones calculated for an infinitely extended image, *i.e.* when $\hat{W}_0(\mathbf{q}) \simeq \delta(\mathbf{q})$. In fact, only in the latter case the intermediate scattering function is given by $f(\mathbf{q}, \Delta t) = f_\infty(\mathbf{q}, \Delta t)$. In all other cases, a mixing between different Fourier components occurs, which for the static amplitude is known as *spectral leakage* in the signal processing literature [25].

To have a physical intuition of why spectral leakage also affects the dynamics, one can consider fig. 1, where simulated real-space images of a spherical particle in different positions (a)–(d) are compared with the corresponding FFT spectra (e)–(h). As far as the particle is well within the image area, the FFT spectrum does not depend on the particle position and it closely mirrors the effective shape factor $P(q)$. When the particle reaches the image boundary, instead (panel 1(c)), a spurious signal is generated, which affects in particular the largest wave vectors, where the amplitude of the "bulk" signal is lower. This extra contribution appears as a "band" localized around the axis and perpendicular to the image boundary, whose amplitude reach a maximum when the particle is cut in half by the image boundary (panel 1(d)). If one thinks of the particle displacement as a dynamical process, the temporal persistence of this extra contribution corresponds to the time needed for the particle to completely cross the boundary (see also supplementary movie M1). In the case of a Brownian particle, this characteristic time can be estimated as $\tau_P \approx \sigma_P^2/D_t$, where D_t is the particle diffusion coefficient and σ_P is the width of its effective shape, which is the largest number between the particle size and the size of the microscope point-spread function. If a large number of particles is imaged, the boundary contribution is expected to be always present and to fluctuate with the same characteristic correlation time τ_P.

To quantitatively assess this effect, we performed a direct numerical integration of eq. (7) for the case of a collection of independent Brownian particles. The shape of the particles is described by a Gaussian profile (with standard deviation σ_P) and the window function W_0 is chosen as the characteristic function of a square with side length N. We assume that the axial dynamics can be neglected, *i.e.* that $f(\mathbf{q}, \Delta t) \simeq f_{2D}(\mathbf{q}, \Delta t) = \exp(-D_t q^2 \Delta t)$.

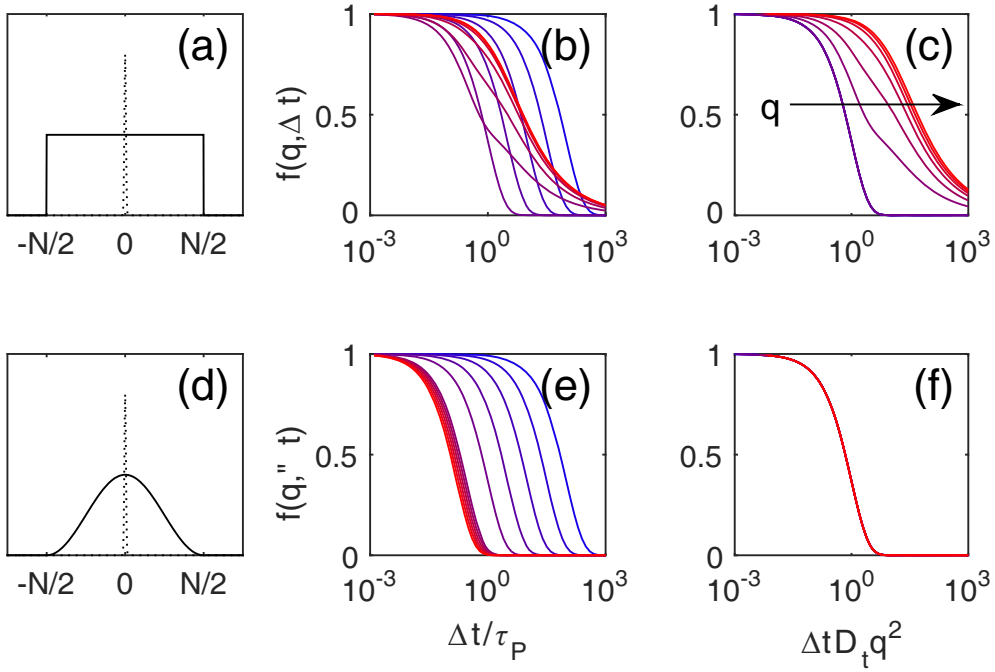

Fig. 2. Results obtained by numerical integration of eq. (7) in the case of Brownian particles with Gaussian effective shape with standard deviation $\sigma_P = 0.05N$ (dotted profile in panels (a) and (d)). The image size is assumed to be N pixels. In the absence of explicit windowing, the window function coincides with the characteristic function of the image area (continuous line in panel (a)). In panel (b) the corresponding normalized intermediate scattering functions for different qs in the range $0.1\sigma_P^{-1} < q < 4\sigma_P^{-1}$ are shown as a function of the dimensionless time delay $\Delta t/\tau_P$, where $\tau_P = \sigma_P^2/D_t$ is the characteristic self-diffusion time of the particle (see main text for details). For large q, the curves converge to a q-independent decay. Such deviation from the expected exponential behavior $f(q, \Delta t) = \exp(-D_t q^2 \Delta t)$ is made evident in panel (c), where the same curves are plotted as a function of the rescaled time $\Delta t D_t q^2$. The application of a smooth window function (continuous curve in panel (d), see also eq. (10)) substantially reduces the spurious effects on the dynamics, as shown in panels (e), (f) where the corresponding normalized intermediate scattering functions are shown for the same q values considered in panels (b), (c). The collapse in panel (f) means that all of the intermediate scattering functions have the same functional form, the exponential decay.

As a consequence of the spectral leakage, we find that for $q > 1/\sigma_P$ the intermediate scattering functions are no longer described by a simple exponential function and tend to decay with a q-independent characteristic time $\tau_P \approx \sigma_P^2/D_t$ (fig. 2(b)).

Our simulations indicate that these *dynamic* artifacts can be avoided if one employs the same windowing procedure that is popular in the signal processing community for the removal of spurious *static* signal correlations [19, 25]. Windowing consists in multiplying the data, before performing the FFT operation, by a window function, usually a symmetric, bell-shaped profile that smoothly goes to zero at both ends of the sampling interval. In this way, the virtual periodic signal that the FFT algorithm produces by combining an infinite collection of replicas of the original image is no longer discontinuous at the boundaries between tiles. In our case, we find that spatial windowing (fig. 2(d)) has a dramatic effect on the reconstructed dynamics (fig. 2(e), (f)): all the intermediate scattering functions that were previously shown to be corrupted by finite-size artifacts, now display a clean exponential relaxation with the expected relaxation rate $\Gamma(q) = D_t q^2$.

The spatial window function chosen in the numerical calculations above and also used in the rest of this article is a Blackman-Harris window function $W_{BN}(x)W_{BN}(y)$, a generalized cosine window function whose 1D version reads [25]:

$$W_{BN}(x) = \sum_{j=0}^{3} (-1)^j a_j \cos\left(\frac{2\pi j x}{L}\right), \qquad (10)$$

where the values of the a_j parameters are fixed. More specifically, they are $a_0 = 0.3635819$, $a_1 = 0.4891775$, $a_2 = 0.1365995$, $a_3 = 0.0106411$ [25]. Both for simulations and experiments, we have also tested other options for the window function, in particular the Hann and Dolph-Chebyshev windowing functions [25]. In both cases, we obtained results equivalent to those obtained with the Blackman-Harris function. We will further comment on this issue in the next Section.

3 Spatial windowing in dynamic microscopy experiments

To assess the validity of the proposed approach in real experiments, we evaluate in this section the effect of spatial windowing on experimental data acquired with bright-field and confocal microscopy. We will show that spatial

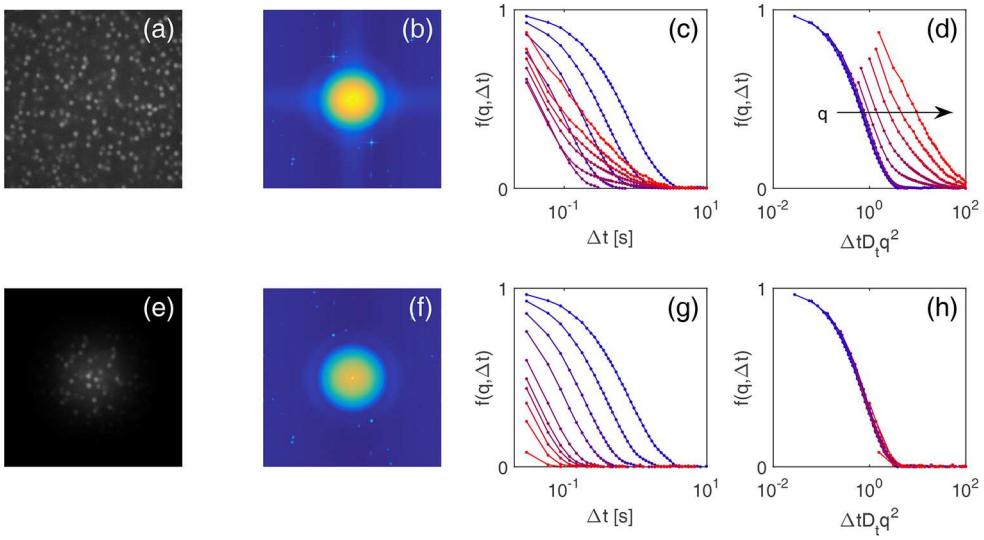

Fig. 3. (a) Representative raw confocal image of a semi-diluted suspension of hard-sphere colloidal particles (see main text for details). (b) 2D image structure function $D(\mathbf{q}, \Delta t)$ for $\Delta t \simeq 20\,\mathrm{s}$, showing the characteristic "bands" along the axes due to spectral leakage. In addition, some bright cross-hairs/dots are also visible that are due to the scanning disk acquisition. The data that correspond to these cross-hairs/dots are excluded from the DDM analysis. (c) Azimuthally averaged intermediate scattering functions as a function of the time delay Δt for different values of the wave vectors q in the range $2\,\mu\mathrm{m}^{-1} < q < 15\,\mu\mathrm{m}^{-1}$. (d) Same as in panel (c), but as a function of the rescaled time delay $\Delta t D_t q^2$. The fact that, at large q, the curves fail to collapse indicates that the spurious dynamics becomes dominant. (e) Same image shown in panel (a) after spatial windowing with a Blackman-Harris window function (eq. (10)). (f) 2D image structure function for $\Delta t \simeq 20\,\mathrm{s}$ as obtained from the windowed image sequence, showing a nice azimuthal symmetry and no bands. The azimuthally-averaged intermediate scattering functions are plotted as a function of the time delay Δt in panel (g) and of the rescaled time delay $\Delta t D_t q^2$ in panel (h), for the same q-values considered in panels (c), (d). After windowing, the intermediate scattering functions do not show any significant deviation from a purely exponential relaxation with diffusive scaling of the relaxation rate $\Gamma(q) = D_t q^2$.

windowing of the images before performing the standard DDM analysis drastically reduces the impact of boundary-related artifacts on both the statics and the dynamics. To focus on the dynamics, we will show in the following experimental results obtained with and without windowing for the intermediate scattering function $f(q, \Delta t)$. Such estimate is obtained by assuming a functional form for $f(q, \Delta t)$ and fitting the $D(q, \Delta t)$ experimental data to eq. (2). Such fit, performed with a custom MATLAB routine, provides also estimates for $A(q)$ and $B(q)$.

3.1 Confocal microscopy

The sample is a semi-diluted (0.04 volume fraction) suspension of sterically stabilized polymethylmethacrylate (PMMA) $0.5\,\mu\mathrm{m}$ fluorescent particles in a density– and refractive-index–matching solvent [6]. The suspension is imaged by a confocal microscope equipped with a Nipkow disk (Yokogawa), a CCD camera (QImaging), a 100X oil immersion objective (Leica), and a solid-state laser source (Laserglow). Image sequences of a single plane from a depth of $20\,\mu\mathrm{m}$ from the lower coverslip are acquired at a frame rate $1/\Delta t_0 = 33.9\,\mathrm{fr/s}$. Image size is 256×256 pixels, with an effective pixel size of 127 nm.

A representative image of the suspension is shown in fig. 3(a). The corresponding two-dimensional image structure function for a large time delay $\Delta t = 20\,\mathrm{s}$ (fig. 3(b)) shows marked artifacts, mainly localized along the horizontal and the vertical axis, that are due to spectral leakage. The impact on the dynamics of the edge-effects can be well appreciated from fig. 3(c), (d), where the intermediate scattering functions obtained from the DDM analysis are shown for different values of q in the range $2\,\mu\mathrm{m}^{-1} < q < 15\,\mu\mathrm{m}^{-1}$. Some of the curves appear non-exponential when plotted as a function of the time delay Δt (panel c) and do not collapse on a unique master curve when plotted as a function of $\Delta t D_t q^2$ (panel d).

The effectiveness of windowing in amending these effects can be appreciated in fig. 3(e)–(h). A representative 2D structure function obtained for the time delay $\Delta t = 20\,\mathrm{s}$ by analyzing windowed images such as the one in fig. 3(e) is shown in fig. 3(f). It is evident that the expected azimuthal symmetry is recovered. In addition, the temporal dependence of the intermediate scattering functions at different q now exhibits the expected exponential decay, with a rate $\Gamma(q) \simeq D_t q^2$ (fig. 3(g), (h)).

To better compare the results of the standard DDM analysis with those obtained by prior windowing of the images, we show in fig. 4 the relaxation rate $\Gamma(q)$ obtained by fitting the intermediate scattering functions in fig. 3(c) and (g) with the model $f(q, \Delta t) = \frac{e^{-\Gamma(q)\Delta t}}{\sqrt{1+\gamma \Delta t}}$. In this expression, obtained by assuming an isotropic diffusive dynamics and a Gaussian-Lorentzian model for the confocal point-spread function [16,6], the denominator accounts for the

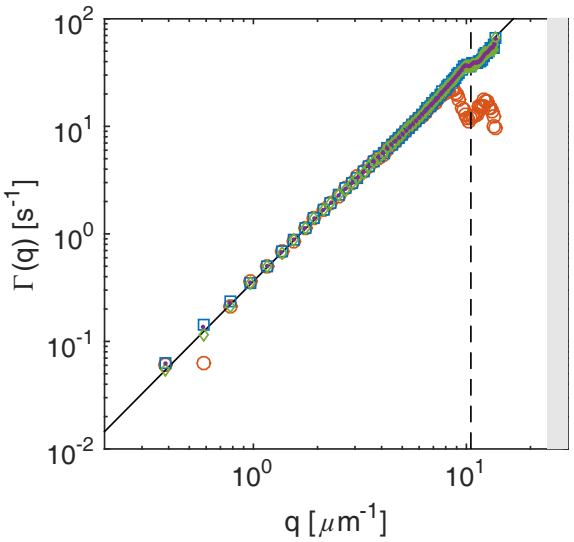

Fig. 4. q-dependent correlation rate $\Gamma(q)$ obtained from the fit of the intermediate scattering function with and without (orange circles) spatial windowing in a confocal microscopy experiment on a semi-diluted suspension of $\simeq$ 500 nm colloidal particles (see text for details). Different symbols correspond to different choices of the window functions (blue square: Blackman-Harris, green diamonds: Hann, purple dots: Dolph-Chebyshev with sidelobe attenuation equal to -100 dB). The vertical dashed line is drawn in correspondence of the position of the calculated first minimum of the shape factor $q^* \simeq 4.4934/R$, where R is the particle's radius. The gray area indicates the wave vector range $q > 4\pi NA/\lambda \simeq 24\,\mu m^{-1}$ falling below the diffraction limit.

axial dynamics and the q-independent rate γ is the one associated with the diffusion across the confocal optical section [16,6]. If we focus only on the horizontal dynamics, the obtained values for $\Gamma(q)$, both in the absence and in the presence of windowing, are compared in fig. 4. In the absence of windowing, a systematic deviation from the expected scaling $\Gamma(q) = D_t q^2$ is observed for $q > 8.5\,\mu m^{-1}$, where a sudden drop is observed. On the contrary, windowing allows the reliable reconstruction of the dynamics up to $q \simeq 16\,\mu m^{-1}$, a limit determined only by the acquisition frame rate that inhibits the access to timescales shorter that about Δt_0. Remarkably, the three windowing functions that we tested give very similar results.

Interestingly, the increased wave vector range made available by the windowing procedure is such that a minimum in the static amplitude is now visible for $q^* \simeq 10.5\,\mu m^{-1}$. This minimum, corresponding to the dark ring around the central lobe of the Fourier spectrum in fig. 3(f), may be attributed to a zero in the particle's form factor. For a sphere of radius R^* the first zero in the from factor is expected to occur for $q^* = 4.4934/R^*$ [20], which provides the estimate $R^* = 4.4934/q^* \simeq 0.44\,\mu m$ for our particles. This value is smaller than the one obtained with the same particles in a previous study [6], where a series of measurements were performed for different volume fractions in the range $0.005 < \phi < 0.4$. In ref. [6], by measuring the diffusion coefficient in a very dilute sample the estimate $R_H = 0.505\,\mu m$ was obtained for the particle's hydrodynamic radius. This value was also found to be in good agreement with the size obtained from the Percus-Yevick fit of the static structure factors of the hard spheres. The observed difference may be attributed to the known fact that for these particles the optical signal is generated by the emission of a fluorescent dye that is physically trapped within the particle itself, in a region that is smaller than the physical size of the particle [8]. For this reason, R^* provides an estimate of the size of the fluorescent portion of the particle.

The improved visibility of the minimum in the static amplitude is accompanied by its dynamical counterpart, which brings in additional physics. Careful inspection of the behavior of $\Gamma(q)$ in the vicinity of q^* (fig. 5(a)) reveals the presence of a characteristic swing on top of the average diffusive scaling $D_t q^2$, consisting in a slight speed up of the dynamics for $q < q^*$, followed by a slowing down for $q > q^*$. This effect has been predicted and observed in the context of dynamic light scattering and can be ascribed to the polydispersity of the particles [20,21]. The normalized fluctuation $D_0 q^2/\Gamma(q)$ is well fitted to the expression given in eq. (33) in ref. [20] from which a polydispersity σ of about 10% can be estimated (fig. 5(c)). This value is larger than the expected particle batch polydispersity, which in our case is estimated to be of the order of 5%. This discrepancy is not surprising because of the non-uniform internal distribution of the dye in our particles [8].

We note that, although windowing increases the accessible wave vector range, this comes at the expenses of the overall signal. As a matter of fact, the application of a window function suppresses a fraction of the intensity in the image, causing a decrease in the measured amplitude $A(q)$ (of about 85%, 75% and 85% for the Blackmann-Harris, Hann and Dolph-Chebyshev functions, respectively), as shown in fig. 5(b).

3.2 Bright-field microscopy

To test the generality of the proposed approach with respect to the imaging contrast mechanism, we applied the same procedure described in the previous paragraph to data obtained with bright-field microscopy. We used two samples: a very diluted suspension of colloidal particles and a binary mixture close to its critical consolution point.

Colloidal suspension

We chose a suspension of monodisperse polystyrene colloidal particles of nominal radius $R = 230 \pm 10$ nm and volume fraction $\phi \simeq 0.0014$ in a dispersing medium made of water (51.2% w/w) and glycerol. Bright-field images are collected with a water immersion objective ($40X$, $NA = 1.15$) mounted on an inverted microscope (Nikon Eclipse). The microscope is equipped with a fast CMOS camera (Hamamatsu ORCA Flash4 V2, effective pixel size $0.163\,\mu m$). Sequences of images were acquired with frame

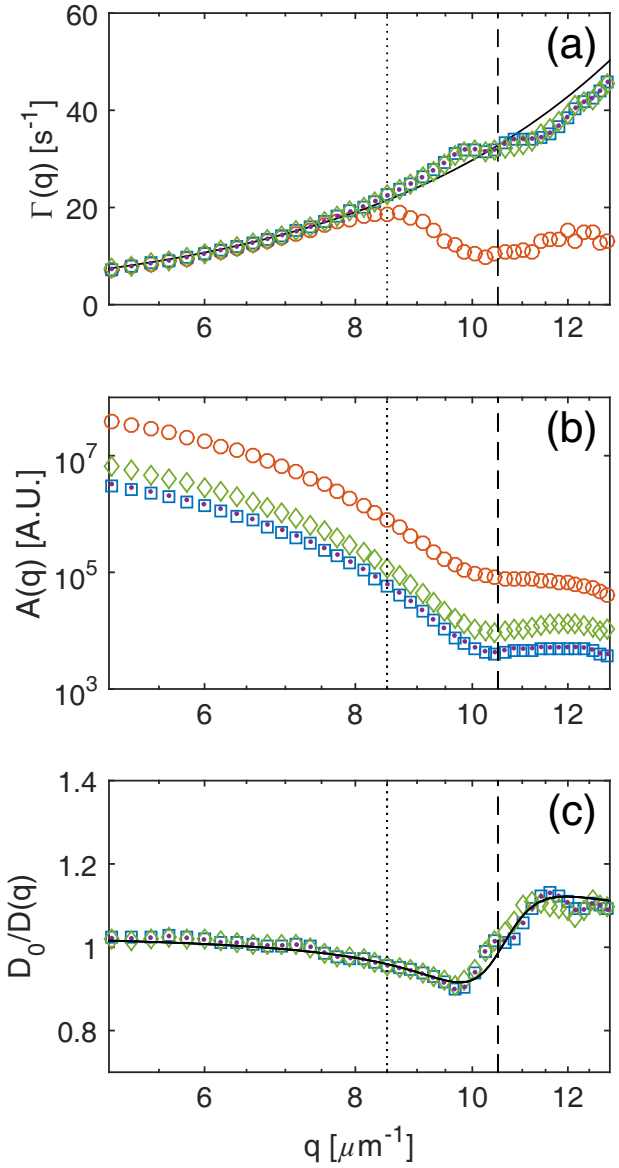

Fig. 5. (a) q-dependent decorrelation rates $\Gamma(q)$ obtained from the fit of the intermediate scattering function, with and without (orange circles) spatial windowing using the window functions (blue square: Blackman-Harris, green diamonds: Hann, purple dots: Dolph-Chebyshev with sidelobe attenuation equal to $-100\,\mathrm{dB}$) in a confocal microscopy experiment on a semi-diluted colloidal suspension (see text for details). The continuous line is the best-fit curve to the data with a quadratic function; the vertical dotted line, drawn for $q = 8.5\,\mu\mathrm{m}^{-1}$, marks where the curve $\Gamma(q)$, obtained without windowing, starts deviating significantly from the expected scaling. (b) Amplitude $A(q)$ obtained from the fit of the intermediate scattering function. Symbols are as in (a). In the presence of windowing, the amplitude is reduced by about 75% (Hann) and 85% (Dolph-Chebyshev and Blackmann-Harris) (c) Ratio between the effective, q-dependent diffusion coefficient $D_t(q) = \Gamma(q)/q^2$ and its mean value D_0 (symbols as in (a)); the continuous line is a best fit of the data to eq. (33) in ref. [20]. The inflection point in $D_0/D_t(q)$ occurs for $q^* = 10.5\,\mu\mathrm{m}^{-1}$, in very good agreement with the position of the first minimum in $A(q)$ (vertical dashed line in all panels).

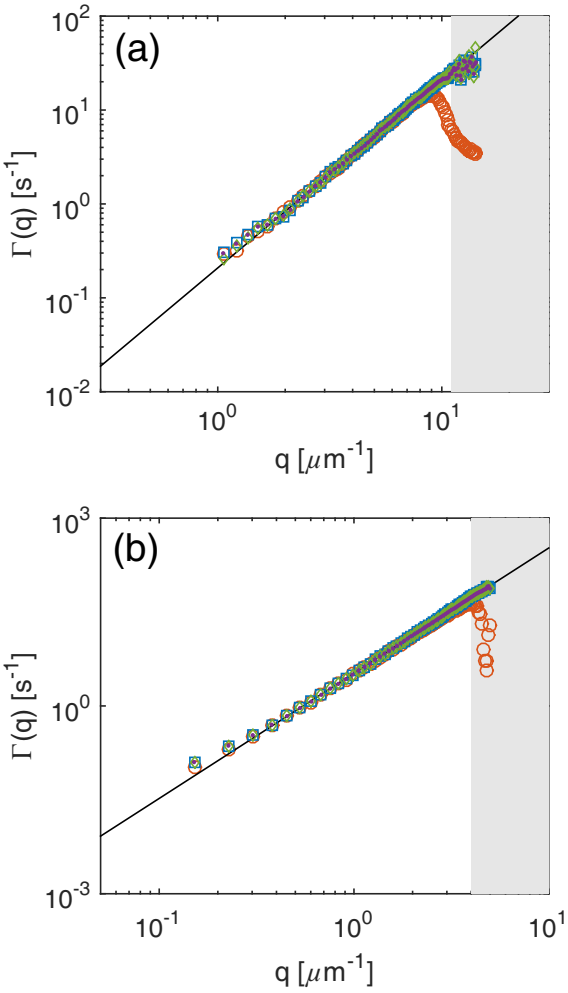

Fig. 6. q-dependent correlation rates $\Gamma(q)$ obtained from the fit of the intermediate scattering function with and without (orange circles) spatial windowing for the two bright-field microscopy experiments described in the main text: (a) a diluted suspension of $\simeq 230\,\mathrm{nm}$ polystyrene particles and (b) a critical binary mixture close to its consolution point. In both panels, different symbols correspond to different choices of the window functions (blue square: Blackman-Harris; green diamonds: Hann; purple dots: Dolph-Chebyshev with sidelobe attenuation equal to $-100\,\mathrm{dB}$), while the gray area indicates the wave vector range $q > 2\pi NA/\lambda$ falling below the diffraction limit.

rate $1/\Delta t_0 = 777\,\mathrm{s}^{-1}$. DDM analysis was performed both on temporal sequences of raw images and of windowed images.

Fitting the temporal dependence of the azimuthally-averaged image structure functions $D(q, \Delta t)$ with a simple exponential decay provides the q-dependent relaxation rates $\Gamma(q)$ shown in fig. 6(a). Fitting of the data for $q \ll 9\,\mu\mathrm{m}^{-1}$ with $\Gamma(q) = D_t q^2$ provides the estimate $D_t = 0.208 \pm 0.005\,\mu\mathrm{m}^{-1}$. For $q > 9\,\mu\mathrm{m}^{-1}$, we observe that the results obtained without windowing deviate systematically from the expected diffusive scaling $\Gamma(q) = D_t q^2$. Such deviation is due to the increasing relevance of the spurious, q-independent dynamics of the particles that diffuse in and out of the region of interest across its edges.

The characteristic rate of the latter process can be roughly estimated as $\tau_P^{-1} \simeq D_t/\sigma_P^2 \simeq 3\,\mathrm{s}^{-1}$, which is compatible with the saturation trend observed for the largest q in fig. 6(a). We note that for the previous estimate we have used $\sigma_P \simeq \lambda/(2NA) \simeq 0.26\,\mu\mathrm{m}$, our particle size being close to the diffraction limit.

On the contrary, the analysis of the windowed sequence provides consistent results up to $q \simeq 14\,\mu\mathrm{m}^{-1}$, this limit being only set by the signal-to-noise ratio. Indeed, the amplitude $A(q)$ is about 400 times smaller than the noise $B(q)$ for $q \simeq 14\,\mu\mathrm{m}^{-1}$. The reliable extraction of quantitative static and dynamic information under this rather unfavorable signal-to-noise ratio is made possible by the use of windowing, which rejects efficiently the finite image-size artifacts. Without windowing the dynamics becomes corrupted as soon as the amplitude of signal falls below the noise level, as spectral leakage effects dominate the signal.

Molecular liquid

Thermally-excited concentration fluctuations in a binary mixture are difficult to probe with visible light, mostly because their amplitude is usually very small. A notable exception is represented by the case of a mixture that is brought close to a critical point, condition in which the concentration fluctuations develop long-range correlations that make both their amplitude and their correlation length incredibly large. Despite its dramatic increase close to a critical point, in typical experimental conditions the correlation length always remains well below the optical resolution, providing us with the ideal sample for assessing the validity of image windowing in sample where the intensity fluctuations are originated by small-size density fluctuations.

To this aim, we have analyzed bright-field movies (Nikon Ti-U, Hamamatsu ORCA-Flash4.0, 2×2 binning, $20\times$ magnification, 50000 images, 128×128 pixels, 200 fps). We show in fig. 6(b) results obtained at a temperature $T = 0.1\,^\circ\mathrm{C}$ above the critical temperature $T_c \simeq 30\,^\circ\mathrm{C}$ in a mixture aniline-cyclohexane prepared at the critical composition (aniline concentration $c_c = 0.47\,\mathrm{w/w}$) [9]. Without windowing (circles), the relaxation rate exhibits a sudden decrease of the experimental relaxation rate that is likely due to the edge-effects described in this work. This is confirmed by application of the windowing procedure, which is found to effectively remove this artifact, with no substantial differences between the three windowing functions tested (squares, diamonds and dots in fig. 6(b)).

The fact that edge-related artifacts arise also when the individual scattering objects are molecules should not surprise because, as also described in sect. 2, the characteristic length-scale of the problem is the largest quantity between the particle size and the optical resolution width of the microscope. This distinction can be appreciated by inspecting figs. 4 and 6: when the individual scattering entities are large (fig. 4), the edge-induced artifact occurs for $q \simeq q^*$, whereas when they are small (fig. 6), the onset of the edge effects is set by the resolution width $2\pi NA/\lambda$.

As a consequence, we expect that the observed effect should be present also in off-critical samples, provided that the amplitude of concentration fluctuations is large enough to generate a detectable signal.

4 Conclusion

We have demonstrated that, in a DDM experiment, particles crossing the boundaries of the images limit and distort the genuine dynamics at high-q. Notably, this happens also when the intensity fluctuations in the microscope images are originated by density fluctuations in molecular fluids. The associated q-independent dynamic signal leads to a spurious suppression of the relaxation rates measured at large q. This peculiar feature appears in several DDM-related investigations (*e.g.*, in refs. [4,18,26]), and has thus far not yet been explicitly discussed, nor its origin investigated or explained. In response, we propose a simple solution —applying a smooth window function to the images before the standard Fourier processing, which despite its conceptual and computational simplicity, significantly enhances the DDM analysis and extends the q-range over which meaningful, reliable estimates of the statics and of the dynamics are obtained. However, our solution may have some potential limitations. For example, we have observed (see for example fig. 5(b)) that image windowing by using the Blackmann-Harris function causes an overall decrease in signal of about 85%. Similarly, the decrease amounts to 75% and 85% for the Hann and Dolph-Chebyshev functions, respectively. Also, a "line broadening" effect is observed as a consequence of the fact that multiplication with the window function in real space leads to convolution with its Fourier transform in the reciprocal domain [19]. In general, we expect that both intensity loss and broadening will not lead to serious consequences in most practical cases, because both the static amplitude $A(q)$ and the intermediate scattering function $f(q, \Delta t)$ are smooth functions of q. In particular, for all the cases studied here we have not observed any artifacts from the use of windowing, also for the smallest wave vectors corresponding to the width of the window function. Consequently, we believe applying a smooth window function as a preprocessing step before Fourier analysis should be an integral part of most DDM implementations, and may also have positive impact in other digital Fourier Microscopy methods [16], such as near-field scattering or shadowgraphy. In particular, we have recently shown that windowing can extend the wave vector range in DDM microrheology experiments, providing a more robust determination of the viscoelastic moduli of complex fluids [27].

This work was supported in part by the Italian Ministry of University and Scientific Research (MIUR) (Project RBFR125H0M); Regione Lombardia; the CARIPLO foundation (Project 2016-0998); NASA (NNX13AQ48G); the National Science Foundation (DMR-1310266); and the Harvard Materials Research Science and Engineering Center (DMR-1420570).

Author contribution statement

FG and RC designed research. PE and PJL performed experiments. All authors discussed the experimental results. FG performed simulations and analyzed the data. PJL, FG and RC wrote the paper.

References

1. R. Cerbino, P. Cicuta, J. Chem. Phys. **147**, 110901 (2017).
2. R. Cerbino, V. Trappe, Phys. Rev. Lett. **100**, 188102 (2008).
3. A.V. Bayles, T.M. Squires, M.E. Helgeson, Soft Matter **12**, 2440 (2016).
4. M. Reufer, V.A. Martinez, P. Schurtenberger, W.C.K. Poon, Langmuir **28**, 4618 (2012).
5. F. Giavazzi, C. Haro-Pérez, R. Cerbino, J. Phys.: Condens. Matter **28**, 195201 (2016).
6. P.J. Lu, F. Giavazzi, T.E. Angelini, E. Zaccarelli, F. Jargstorff, A.B. Schofield, J.N. Wilking, M.B. Romanowsky, D.A. Weitz, R. Cerbino, Phys. Rev. Lett. **108**, 218103 (2012).
7. T. Sentjabrskaja, E. Zaccarelli, C.D. Michele, F. Sciortino, P. Tartaglia, T. Voigtmann, S.U. Egelhaaf, M. Laurati, Nat. Commun. **7**, 11133 (2016).
8. T.E. Kodger, P.J. Lu, G.R. Wiseman, D.A. Weitz, Langmuir **33**, 6382 (2017).
9. F. Giavazzi, A. Fornasieri, A. Vailati, R. Cerbino, Eur. Phys. J. E **39**, 103 (2016).
10. F. Giavazzi, G. Savorana, A. Vailati, R. Cerbino, Soft Matter **12**, 6588 (2016).
11. F. Giavazzi, S. Crotti, A. Speciale, F. Serra, G. Zanchetta, V. Trappe, M. Buscaglia, T. Bellini, R. Cerbino, Soft Matter **10**, 3938 (2014).
12. L.G. Wilson, V.A. Martinez, J. Schwarz-Linek, J. Tailleur, G. Bryant, P. Pusey, W.C. Poon, Phys. Rev. Lett. **106**, 018101 (2011).
13. V.A. Martinez, R. Besseling, O.A. Croze, J. Tailleur, M. Reufer, J. Schwarz-Linek, L.G. Wilson, M.A. Bees, W.C.K. Poon, Biophys. J. **103**, 1637 (2012).
14. M. Drechsler, F. Giavazzi, R. Cerbino, I.M. Palacios, to be published in Nat. Commun. (2017).
15. L. Feriani, M. Juenet, C.J. Fowler, N. Bruot, Biophys. J. **113**, 109 (2017).
16. F. Giavazzi, R. Cerbino, J. Opt. **16**, 083001 (2014).
17. K. He, M. Spannuth, J.C. Conrad, R. Krishnamoorti, Soft Matter **8**, 11933 (2012).
18. D.M. Wulstein, K.E. Regan, R.M. Robertson-Anderson, R. McGorty, Opt. Express **24**, 20881 (2016).
19. R. Priemer, *Introductory Signal Processing* (World Scientific, 1990).
20. P.N. Pusey, W. van Megen, J. Chem. Phys. **80**, 3513 (1984).
21. H. Schöpe, O. Marnette, W. Van Megen, G. Bryant, Langmuir **23**, 11534 (2007).
22. F. Croccolo, D. Brogioli, A. Vailati, M. Giglio, D.S. Cannell, S.S. Sadhal, Ann. N.Y. Acad. Sci. **1077**, 365 (2006).
23. F. Giavazzi, D. Brogioli, V. Trappe, T. Bellini, R. Cerbino, Phys. Rev. E **80**, 031403 (2009).
24. B.J. Berne, R. Pecora, *Dynamic Light Scattering: With Applications to Chemistry, Biology, and Physics* (Dover Publications, 2000).
25. F.J. Harris, Proc. IEEE **66**, 51 (1978).
26. D. Germain, M. Leocmach, T. Gibaud, Am. J. Phys. **84**, 202 (2016).
27. P. Edera, D. Bergamini, V. Trappe, F. Giavazzi, R. Cerbino, arXiv preprint:1708.07170 (2017).